



Design, fabrication, and testing of an X-band 9-MeV standing-wave electron linear accelerator

Jian Gao^{1,2} · Hao Zha^{1,2} · Jia-Ru Shi^{1,2} · Qiang Gao^{1,2} · Xian-Cai Lin^{1,2} · Fang-Jun Hu^{1,2} · Qing-Zhu Li^{1,2} · Huai-Bi Chen^{1,2}

Received: 26 February 2023 / Revised: 3 April 2023 / Accepted: 18 April 2023 / Published online: 28 July 2023

© The Author(s), under exclusive licence to China Science Publishing & Media Ltd. (Science Press), Shanghai Institute of Applied Physics, the Chinese Academy of Sciences, Chinese Nuclear Society 2023

Abstract

In this study, an X-band standing-wave biperiodic linear accelerator was developed for medical radiotherapy that can accelerate electrons to 9 MeV using a 2.4-MW klystron. The structure works at $\pi/2$ mode and adopts magnetic coupling between cavities, generating the appropriate adjacent mode separation of 10 MHz. The accelerator is less than 600-mm long and constitutes four bunching cells and 29 normal cells. Geometry optimizations, full-scale radiofrequency (RF) simulations, and beam dynamics calculations were performed. The accelerator was fabricated and examined using a low-power RF test. The cold test results showed a good agreement with the simulation and actual measurement results. In the high-power RF test, the output beam current, energy spectrum, capture ratio, and spot size at the accelerator exit were measured. With the input power of 2.4 MW, the pulse current was 100 mA, and the output spot root-mean-square radius was approximately 0.5 mm. The output kinetic energy was 9.04 MeV with the spectral FWHM of 3.5%, demonstrating the good performance of this accelerator.

Keywords Standing-wave accelerating structure · RF analysis · Thermal DC gun · Low-power RF test · High-power experiment

1 Introduction

Electron linear accelerators are commonly used in both industry and medicine, i.e., for radiotherapy, nondestructive testing, industrial irradiation, and sterilizing [1]. Currently, most electron linear accelerators operate in the S-band. Their large weight and volume cause various difficulties during testing and installation, such as a lack of space in the operating room for intraoperative irradiation. Linear accelerators operating at C- and X-bands have been proposed to overcome these problems [2, 3, 4].

In recent years, X-band electron linear accelerators have attracted considerable attention worldwide. Compared with S- and C-band linear accelerators, X-band linear accelerators have advantages such as a compact structure, light-weight, and high accelerating gradient. In particular, the Accelerator Laboratory at Tsinghua University has conducted research in this field [5]. Over the past 10 years, S- and C-band standing-wave (SW) linear accelerators driven by domestic magnetrons have been successfully studied [6, 7, 8, 9].

For radiotherapy applications, a narrow energy spread is important because it can significantly affect the dosage rate. The consumption of radiofrequency (RF) power by the linear accelerator is expressed as follows [10]:

$$P_{\text{in}} = \frac{V_m^2}{R_s} + V_a I, \quad (1)$$

where V_m is the maximum kinetic energy, and V_a is the average energy of the accelerated electrons. For the same input power and beam current, a large energy spread leads to a decrease in V_a and an increase in V_m . This energy spread severely decreases the radiation dose rate to a value that is

This work was supported by the Key R&D Project of the Ministry of Science and Technology of China (No. 2022YFC2402300).

✉ Jia-Ru Shi
shij@mail.tsinghua.edu.cn

¹ Department of Engineering Physics, Tsinghua University, Beijing 100084, China

² Key Laboratory of Particle and Radiation Imaging (Tsinghua University), Ministry of Education, Beijing 100084, China

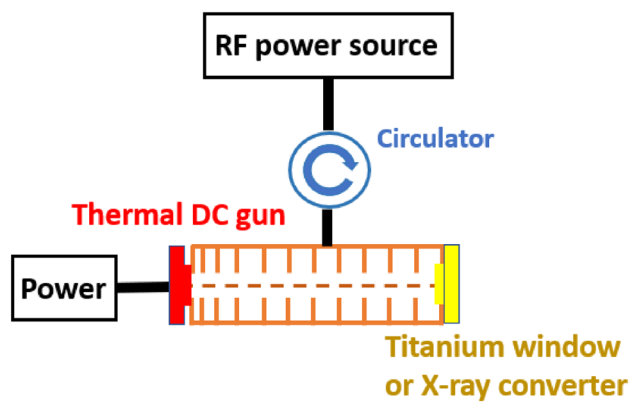


Fig. 1 (Color online) Diagram of standing-wave (SW) electron linear accelerator. RF: radiofrequency

Table 1 Some basic parameters of proposed X-band SW linear accelerator. *RMS* root mean square

Parameter	Value
Number of accelerating cavities	29
Length (m)	0.59
Input RF power (MW)	2.4
Pulse beam current (mA)	100
Capture ratio	32%
RMS beam spot radius (mm)	0.5
Energy dispersion (keV)	250
Average accelerating gradient (MeV/m)	15

unacceptable for radiotherapy. Consequently, medical linear accelerators with narrow energy spreads have attracted significant attention.

With a 2.4-MW input RF power source, we designed a compact X-band SW linear accelerator at Tsinghua University for medical applications, including X-ray and intraoperative electron beam radiotherapies. The design goal was to achieve a 100-mA pulse current with the kinetic energy of 9.0 MeV. The length of the accelerating structure is less than 600 mm. In addition, the SW biperiodic on-axis coupled structure was selected and operated at $\pi/2$ mode and 9.3 GHz. RF focusing was introduced using noses in the accelerating cells, and an external solenoid was unnecessary. A narrow energy spread was achieved using a thermal DC gun and specifically optimized bunching cells. The basic components of a linear accelerator are illustrated in Fig. 1, including an RF power source, circulator, accelerating structure, thermal DC gun, and titanium window. In addition, Table 1 presents some critical parameters of the accelerator.

This low- and high-power accelerator was designed, fabricated, and tested in our laboratory. The frequency of each cell, distribution of the on-axis electric field, and coupling

coefficient were measured during the cold test. The corresponding results are in good agreement with those of our previous simulation. A high-power RF test was conducted to measure the performance of the accelerator, including the output beam current, capture ratio, energy spectrum, size of the beam spot, and breakdown rate (BDR), among other useful data.

This paper presents the RF design, simulation analysis, fabrication, and test results of the proposed SW linear accelerator. The remainder of the paper is organized as follows. In Sect. 2, the RF design and analysis of the X-band accelerating structure are described. The results of the calculations for the electronic gun simulation and beam dynamics are also presented. Section III introduces the fabrication, tuning, and low-power RF testing of the accelerating structure. Section 4 details the setup and results of the high-power RF experiment. Finally, the conclusions and outlook are provided in Sect. 5.

2 RF design and analysis

A high accelerating gradient is necessary to improve the accelerating efficiency and increase the output beam energy without excessive length. The longitudinal shunt impedance of the accelerator is expected to be as large as possible within a reasonable range of the RF BDR. Accordingly, in this study, we aimed to determine a group of appropriate structural parameters to satisfy these requirements simultaneously. For the design process, the cavity geometry was optimized using SUPERFISH, the beam dynamics were investigated using ASTRA, and full-scale RF simulations were performed using CST codes [11, 12].

A. Cavity geometry optimization.

Geometric optimization of normal cells is essential for achieving a high accelerating efficiency. In a linear accelerator, the kinetic energy of an electron gain can be expressed as follows [13]:

$$W = \sqrt{Z_{\text{eff}} PL}, \quad (2)$$

where Z_{eff} represents the effective shunt impedance, P represents the microwave power loss, and L represents the longitudinal length. With increasing Z_{eff} , this accelerator was shortened longitudinally. During cavity geometry optimization, we aimed to obtain the maximum longitudinal shunt impedance. Figure 2 displays the two-dimensional model used for the geometry optimization. An axisymmetric structure can be realized based on two-dimensional models, and the relative RF characteristic parameters can be determined. Further, this method can significantly reduce

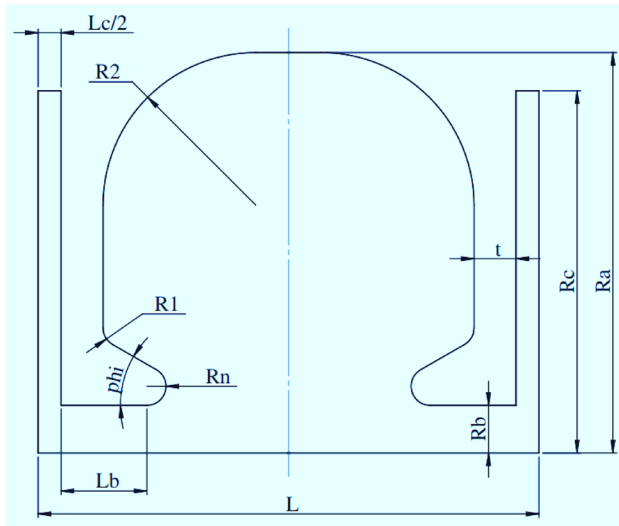


Fig. 2 Two-dimensional model of a normal cell constituting an accelerating cavity and coupling cavity

the optimization time and hence greatly improve efficiency. Reduced coupling cell length and disk thickness will lead to a dramatically improved effective shunt impedance; however, the cavities will easily deform during processing. The beam pipe radius and nose radius are also critical to the longitudinal shunt impedance. However, a small beam pipe radius and nose radius result in a low capture coefficient because more bunches collide with the beam pipe. Moreover, a small nose radius generates a high BDR, and the stability of the accelerator is weakened. Therefore, appropriate values for these parameters were determined.

The $\pi/2$ mode was selected as the working mode of the electron linear accelerator for maximal adjacent mode separation and frequency robustness during operation. According to the biperiodic structure theory, to maximize the longitudinal shunt impedance, the coupling cell should have a small volume and a very weak internal electromagnetic field. In our model, the coupling cells are only 1.5 mm in length; therefore, their effective shunt impedance and quality factor can be ignored.

The RF characteristics of the normal cells are presented in Table 2: f_a indicates the frequency of the accelerating cells, f_c represents the frequency of the coupling cells, Z_{eff} is the effective longitudinal shunt impedance, and Q_0 is the unloaded quality factor.

Table 2 RF characteristics of optimized accelerating and coupling cavities

Parameter	f_a (GHz)	f_c (GHz)	Z_{eff} (M Ω /m)	Q_0
Value	9.3	9.3	165	8900

2 Design and simulation of cavity chain.

As the nose weakens the electric coupling through the beam hole, magnetic coupling was adopted instead. We implemented magnetic coupling slots between the accelerating and coupling cells as portrayed in Fig. 3.

First, the coupling coefficient between cavities was determined. To avoid the sub-adjacent coupling effect, the adjacent magnetic coupling slots were arranged orthogonally, as shown in Fig. 3. The dispersion equation for a coupled cavity chain can be expressed as follows [13]:

$$f_\varphi = \frac{f_0}{\sqrt{1 + k \cos \varphi}}, \tag{3}$$

where k refers to the magnetic coupling coefficient between cavities, and φ is the phase shift between cavities. The separation between adjacent modes of the dominant $\pi/2$ mode must be considered to provide enough bandwidth between them. To achieve this, k should be 2%–3%, as a large value will lead to a loss of accelerating efficiency [12]. According to our calculations, when k was 2.7%, the adjacent mode separation of 10 MHz was obtained. In bunching cavities, the stored power is inversely proportional to the magnetic coupling coefficient [15]. Thus, for bunching cells, we pre-designed a unique on-axis electric field distribution, formed only via modification of the coupling coefficient between bunching cells, to obtain a feasibly high capture rate. The procedure was the same as that for the normal cells described above.

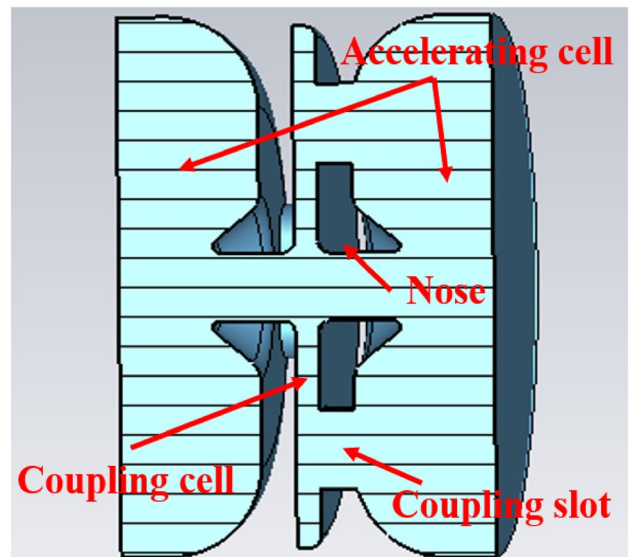


Fig. 3 (Color online) Vacuum model of one normal cell comprising accelerating and coupling cells

3 Design of external coupler and waveguide window.

To feed RF power into the accelerator, an external coupler comprising a unique coupler cell and an external coupling hole was connected to the rectangular waveguide. A vacuum model of the accelerator with a coupler was built into the CST, as shown in Fig. 4. The results, including the on-axis electric field distribution and S_{11} parameter, are displayed in Fig. 5.

The external coupling coefficient is given by [13]:

$$\beta = \frac{Q_0}{Q_e}, \tag{4}$$

where Q_0 is the unloaded quality factor of the accelerating structure, and Q_e refers to the external quality factor. When the beam current was extremely weak, the optimal external coupling coefficient was 1. However, if the beam loading is nonnegligible, the optimum external coupling coefficient can be calculated by [13]:

$$\beta_{opt} = \left(\frac{I}{2} \sqrt{\frac{ZL}{P_0}} + \sqrt{1 + \frac{I^2 ZL}{4P_0}} \right)^2, \tag{5}$$

where I is the output beam current, P_0 is the input power, and ZL are the effective longitudinal shunt impedance and length of the accelerator, respectively. According to our design, the output beam current was approximately 100 mA, the average energy was approximately 9 MeV, and the input RF power was 2.4 MW. Consequently, the optimum external coupling was approximately 1.96.

Waveguide windows such as klystrons, magnetrons, and accelerators are widely incorporated in electric vacuum devices. The functions of the waveguide window are to translate RF power with low loss, and provide isolation between the vacuum within the accelerator and the SF6 inside the waveguide. For this accelerator, we optimized and fabricated a waveguide window based on a 2.4-mm-thick quartz dielectric slice, as shown in Fig. 6.

According to classical transmission line theory, when RF breakdown occurs in the accelerator, the terminal is mismatched, and the incident wave is fully reflected. Currently,

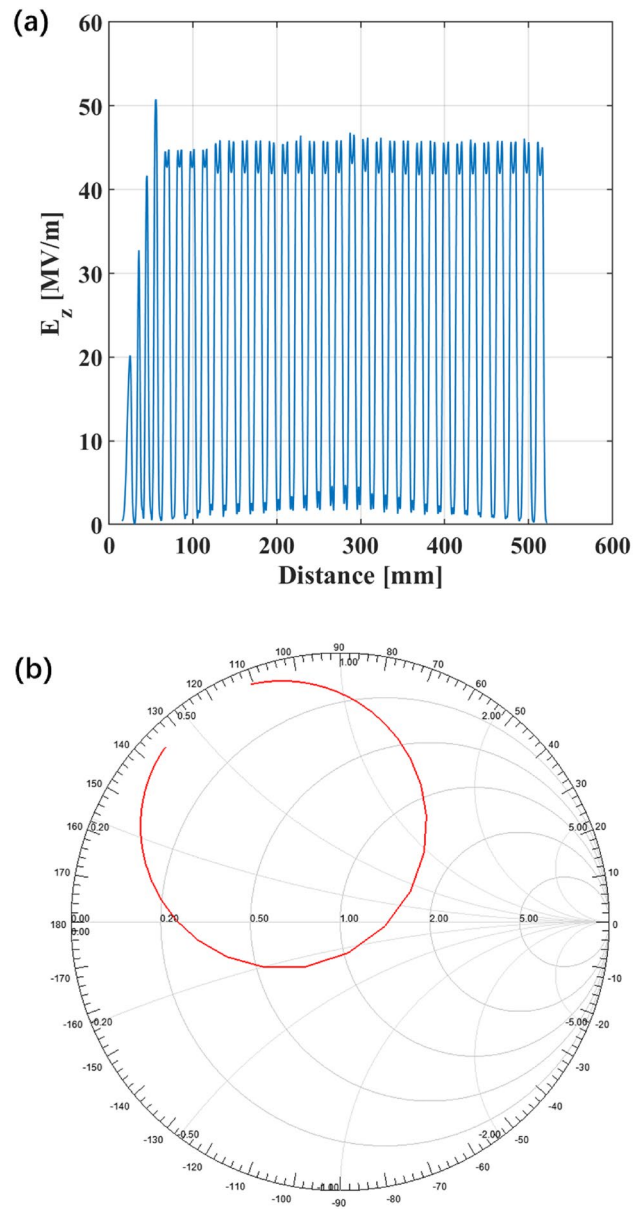


Fig. 5 a Magnitude of on-axis electric field of accelerating structure. b Smith plot of S_{11} parameter for accelerating structure

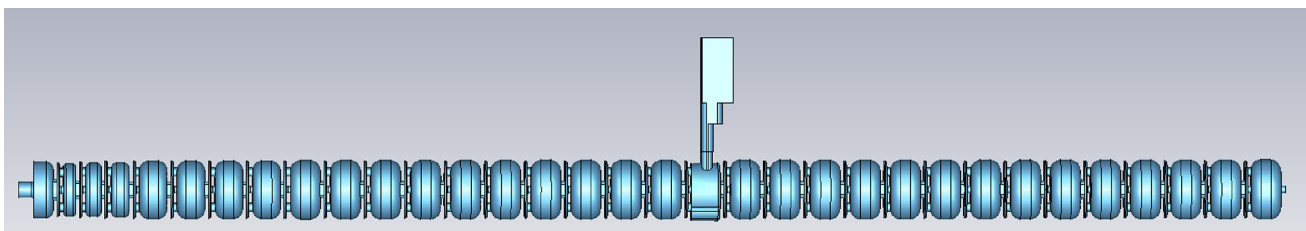


Fig. 4 (Color online) Vacuum model of cavity chain, external coupler, and waveguide for RF simulation in CST

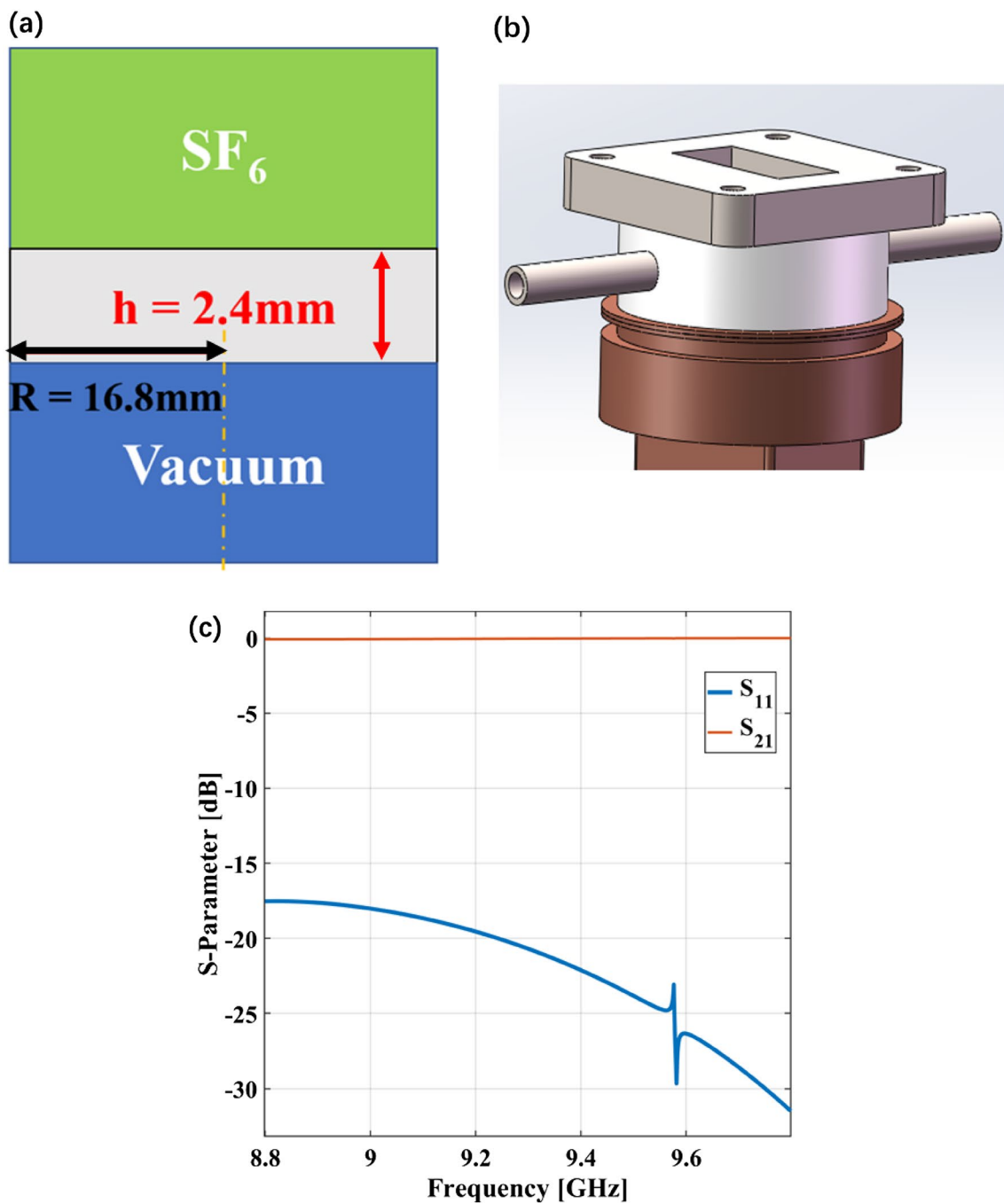


Fig. 6 (Color online) **a** Components of waveguide window system: SF6 (green section) in the waveguide close to the power source and high vacuum (blue section) in the external coupler, separated by quartz slice (gray section). **b** Mechanical design of waveguide window, including copper connector, cooling water pipe, and BJ84 rec-

tangular flange. **c** *S* parameter plots of waveguide window. Blue and orange lines correspond to S_{11} and S_{21} . S_{11} is lower than -20 dB at 9.3 GHz, demonstrating the feasibility of the proposed waveguide window design

transmission waveguides contain SW components. The RF window should be positioned far from the antinode of the SW and near the wave node, as indicated in Fig. 7, to reduce the probability of dielectric breakdown on the surface of the quartz window.

4 Accelerating electric field buildup time.

The field buildup time of an RF structure is closely related to its loaded quality factor. Unloaded quality factor Q_0 of the cavity chain was obtained via CST simulation.

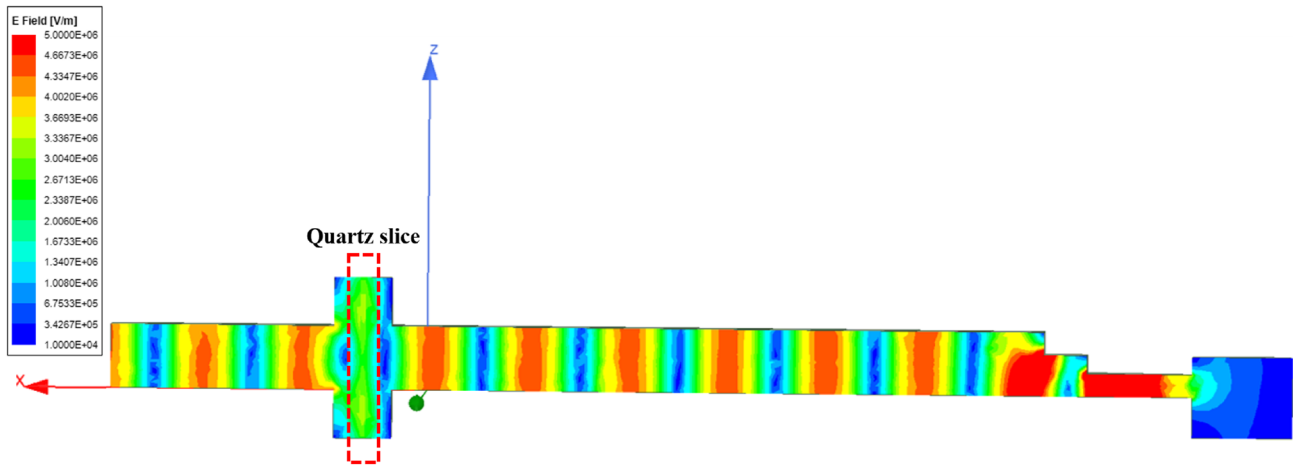


Fig. 7 (Color online) Magnitude of SW electric field inside waveguide and coupler when RF breakdown occurs in accelerator and input RF power is fully reflected

The loaded quality factor can be directly calculated using Q_0 and external coupling coefficient β .

$$Q_L = \frac{Q_0}{1 + \beta} \tag{6}$$

Based on the results of the RF analysis, $-Q_L$ was calculated as approximately 3055. In the field construction process inside the accelerator, basic parameters, such as the electromagnetic field and input impedance within the structure, change exponentially. In particular, the amplitude of the electric field in the cavity increases exponentially with time, as follows:

$$\frac{E}{E_{\text{steady}}} = 1 - e^{-\frac{\omega_0 t}{2Q_L}} = 1 - e^{-\frac{t}{t_F}}. \tag{7}$$

Further, at the end of the transient time $4 \cdot t_F$, the magnitude of the electromagnetic field was calculated to reach approximately 98% of the steady state. During the electromagnetic field construction, the field distribution is time-varying, reaching 9.0 MeV at the steady state. According to theoretical calculations, there exists an optimal injection time t_{opt} at which the injected electron beam is stably accelerated to 9.0 MeV and continues after this time [14].

$$t_{\text{opt}} = \left(\ln \frac{I}{2} \sqrt{\frac{\beta_e P_0}{Z T^2 L}} \right) \cdot t_F. \tag{8}$$

We can obtain that $t_{\text{opt}} \approx 2.46 \cdot t_F$. Compared with the 10- μs microwave macro-pulse width, the transient field buildup time is only 0.27 μs , and can thus be ignored.

3 Simulation of thermal DC gun and beam dynamics

A. Thermal DC gun.

We adopted a thermal cathode DC gun as the electron source, constituting a cathode, heating filament, focusing electrode, anode, insulating ceramic shell, and connector to the accelerator. The emission model was simulated using the CST particle module. The emission current at 12.5-kV high voltage is 320 mA, and the perveance is 0.23 μP . The simulation results and basic parameters are shown in Fig. 8, while the basic parameters of the DC gun are listed in Table 3.

2 Thermal DC gun.

Our design process involved a beam dynamics study using the ASTRA codes. The apertures were carefully set based on the nose position and the radius. We matched the actual accelerating structure and achieved an accurate beam loss calculation. The pulse beam current of 100 mA and capture ratio of 32% were achieved. The results of the beam dynamics calculations are displayed in Fig. 9.

The accelerating structure generates weak RF focusing/defocusing on the electron beams during their transit. Depending on the electric field distribution of the symmetric accelerating cell, the electrons were alternately focused and defocused. However, their momentum is greater when the electrons are focused than when they are defocused, leading to an overall focusing effect.

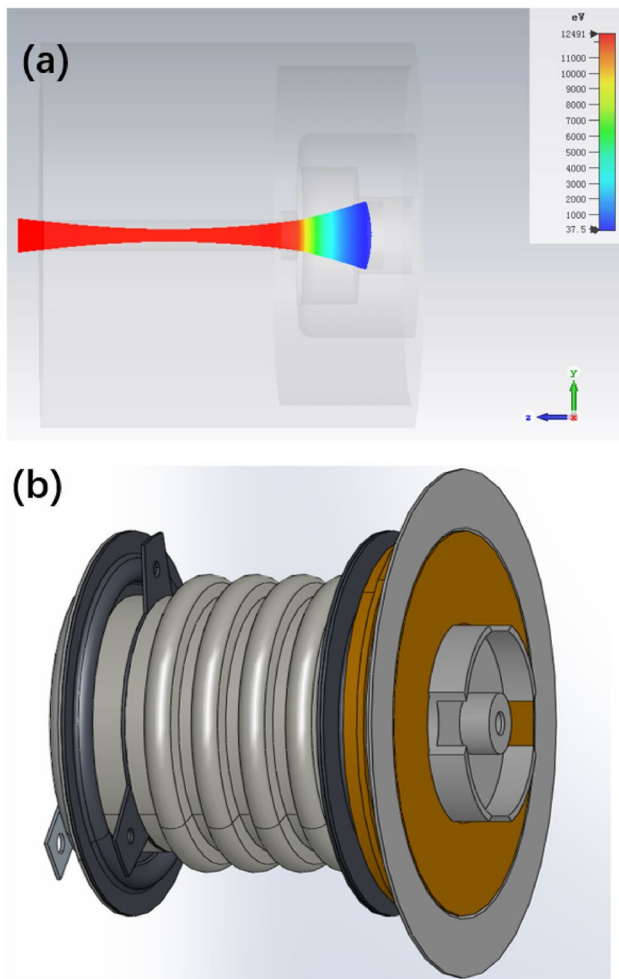


Fig. 8 (Color online) **a** Beam simulation of thermal DC gun in CST. **b** Mechanical design of thermal DC gun

Along the light-speed section, the energy of the accelerating electrons gradually increases, and the space charge force decreases. Benefiting from the RF focusing effect, application of an additional solenoid is unnecessary in our design for reducing the additional space cost and inconvenience. Figure 10 shows the beam spot and the transverse and longitudinal phase-space distributions at the exit of the accelerator.

Table 3 Parameters of thermal cathode DC gun

Parameter	V_e (kV)	I_e (mA)	P_e (μ P)	R_w (mm)	L_w (mm)	R_h (mm)
Value	12.5	320	0.23	0.316	13.05	1.5

V_e high voltage applied between cathode and anode, I_e emission current, P_e gun perveance, R_w RMS radius at beam waist, L_w distance between beam waist and cathode, and R_h beam pipe radius

4 Low-power RF test

Thirty-three pairs of copper disks were manufactured in total, each with four cooling water channels. Owing to their thinness, all copper disks were fabricated without tuning of the holes or pins. Each disk was processed using a smaller cavity radius. After each cold test, unsatisfactory copper disks were reprocessed using a high-precision milling machine. In addition, the structure was reprocessed for cavities with a large deviation away from 9.3 GHz to achieve finetuning. All RF cavities were tuned into an appropriate range around the operating frequency of 9300 ± 5 MHz. An RF cold test was performed at each fabrication step. The test results for the last machining round agreed well with the simulation results.

A few disks and the low-power RF test setup are shown in Fig. 11. The cavity chain was assembled using a fixture, the on-axis field distribution was measured via the bead-pulling method, and the S_{11} data were sampled [15, 16, 17, 18]. The results were compared with our previous simulation results, as shown in Fig. 12. The measured on-axis field distributions are compared in Fig. 5a. The cold test results show a good agreement with the simulation and actual measurement results.

5 High-power RF experiment

A. High-power experiment platform and conditioning.

The assembled cavity chain, waveguide coupler, and quartz waveguide window were brazed with a silver-based alloy. Subsequently, a cooling water pipe, thermal DC gun, and titanium window were welded to the accelerator structure using an argon arc. After vacuum-leak detection and cathode activation of the thermal DC gun, the accelerator structure was complete, as shown in Fig. 13.

Using the waveguide and titanium windows, the vacuum inside the accelerator tube was sealed and isolated from the SF6 gas in the high-power waveguide transmission system. A CF63 flange was installed to connect to the magnetic spectrometer and measure the energy spectrum of the output beam. A titanium getter pump was welded onto the waveguide to maintain low vacuum in the accelerating structure.

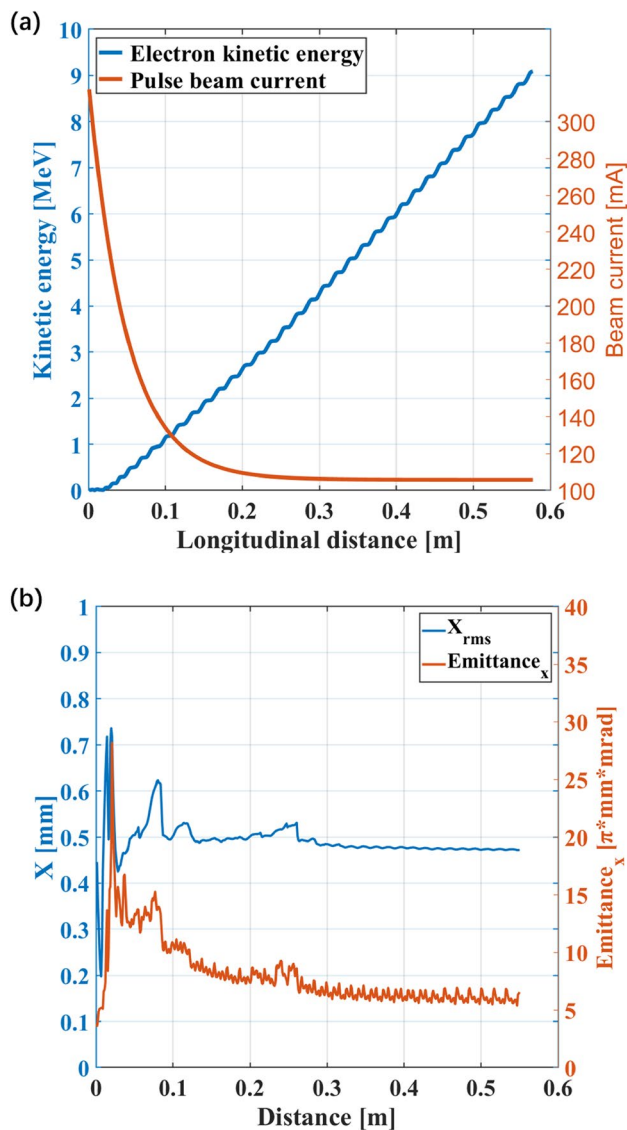


Fig. 9 (Color online) Statistical results of beam dynamics simulation, along the accelerating structure longitudinally: **a** kinetic energy (blue line) and pulse beam current (orange line); **b** RMS beam spot radius (blue line) and transverse beam emittance (orange line)

The vacuum degree of the accelerating structure should remain lower than 10^{-6} Pa. With fixed performance of the thermal DC gun, the corresponding applied high voltage can be adjusted to change the emission current: The emission and pulse beam currents increased as the voltage increased. The mismatch between the initial kinetic energy and accelerating field caused a drop in the capture ratio at excessive voltages (> 13 kV). Therefore, we adjusted the high voltage in the range of 12–13 kV for the high-power experiment.

Subsequently, the RF characteristics of the completed accelerator were determined. For this, the reflection coefficient, SW ratio, quality factor, and external coupling coefficient were calculated. An R&S ZVA60 Vector Network

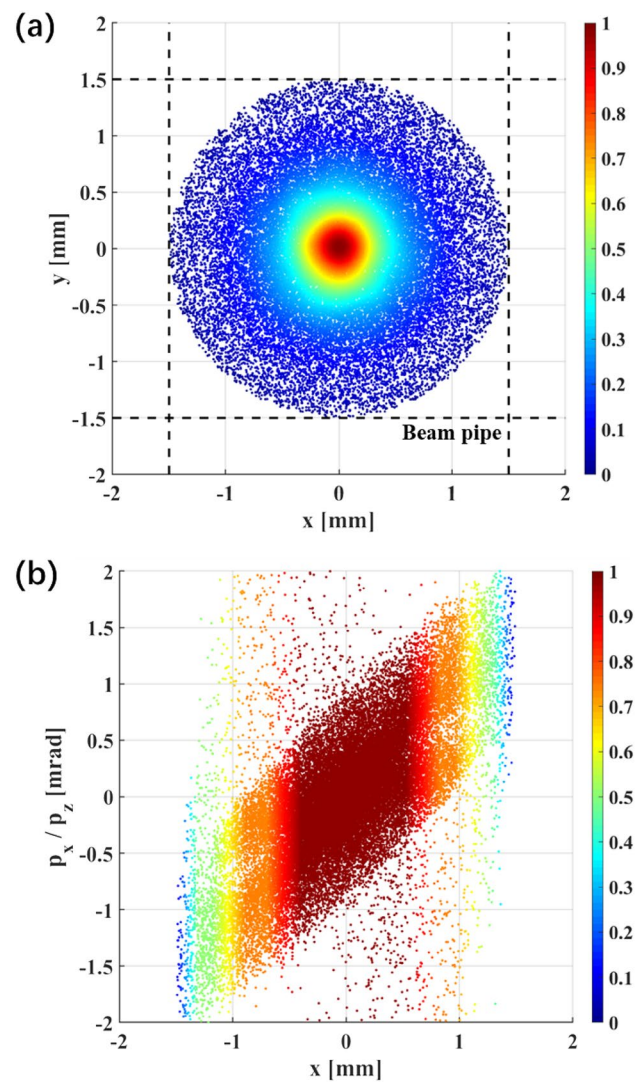


Fig. 10 (Color online) Beam information at the exit of the accelerator, for 10^5 macroparticles during the beam dynamics calculation: **a** transverse beam spot (dashed line is the beam pipe radius of 1.5 mm); and **b** transverse phase space

Analyzer was employed as the measuring instrument. No significant frequency shift was observed after brazing. The simulation results were slightly higher than the external coupling coefficient of 1.8. The reason for this may be an error in the waveguide port calibration before the cold test, as well as the unsatisfactory electrical contact between the waveguide window and measurement port.

Based on a study on the RF breakdown phenomenon of a high-gradient accelerating structure, we know that the RF BDR is closely related to the accelerating gradient and RF pulse width. The relationship between the BDR, accelerating gradient, and pulse width can be expressed as follows [19, 20, 21]:

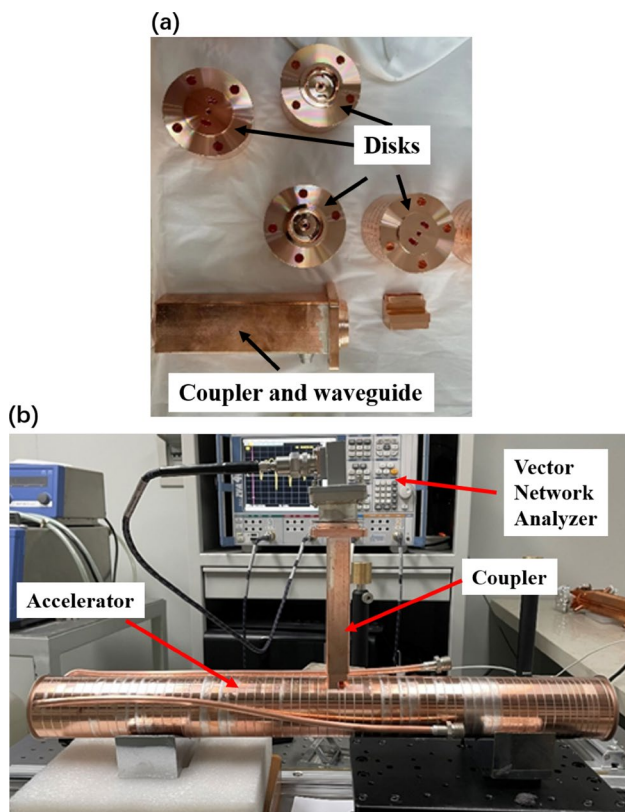


Fig. 11 (Color online) **a** Copper disks, coupler waveguide, and waveguide after fabrication. **b** Picture of low-power RF test setup

$$\frac{BDR}{E_{acc}^{30} t_p^5} = \text{const.} \tag{9}$$

In our high-power experiment, the klystron pulse was long, up to 10 μs , and the ignition rate was high. Moreover, the pulse must be conditioned in advance to reduce the BDR and improve the stability during high-power experiments. The RF power fed into the accelerator was gradually increased. To avoid irreversible damage to the cavity wall, the accelerating structure was fully conditioned to control the BDR below 10^{-4} /pulse, with the input RF power of 2.4 MW [22, 23].

We built a high-power experimental platform to obtain such results for the accelerator. A compact 2.4-MW X-band high-power multibeam klystron was installed as the RF power source to provide input RF power for the accelerator. The circulator separates the klystron and accelerator, and these components are connected by a waveguide filled with high-pressure SF_6 gas. We installed several directional couplers to monitor the incident wave in the accelerator and the wave reflected from the accelerator. To measure the output beam current, a Faraday cup with an integrated circuit was installed at the exit of the accelerator.

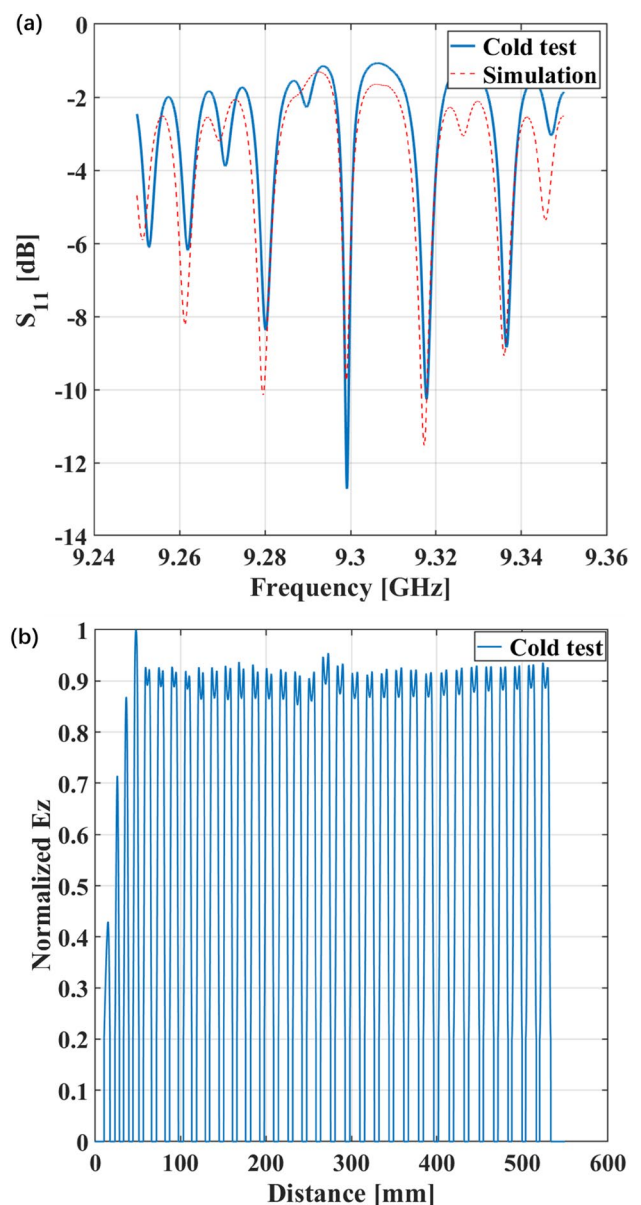


Fig. 12 Low-power RF measurement results for accelerator. **a** Cold test (blue line) and simulated (red line) results for S_{11} parameter. **b** Relative magnitude of on-axis electric field in the cold test

Additionally, a Tektronix DPO4034 oscilloscope was employed to sample electrical signals, including the klystron's emitting current and the collector current of the thermal DC gun, the emission current and high voltage, and the output beam current collected by the Faraday cup. Moreover, the electrical signals were denoised to eliminate high-voltage interference from the high-voltage modulator. A Rohde and Schwarz NRP-Z81 power meter was incorporated to measure the incident and reflected wave signals of the accelerator. The beam current waveform, energy spectrum, capture coefficient, and output beam spot size were measured and evaluated during the high-power experiments.

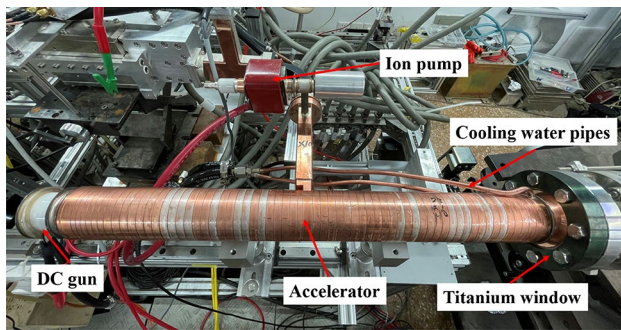


Fig. 13 (Color online) Whole accelerator with all components, including thermal DC gun, titanium window, cooling pipes, and ion pump

2 Results of high-power experiment

The signals of the output beam current and high voltage applied to the thermal DC gun were sampled using a Tektronix DPO4034 oscilloscope. Accordingly, the best data are displayed in Fig. 14, for which the pulse width is $9.8 \mu\text{s}$, the pulse beam current is 100 mA , and the repetition rate is 50 Hz (i.e., the operating duty ratio is 0.5%). Because of some mismatch between the klystron and modulator, the input RF power is not strictly flat and decreases slowly with pulse time. This imperfect input RF pulse causes a slight decline in the waveform of the output beam current. The ratio between the output beam current and emission current from the thermal DC gun was regarded as an approximate estimate of the capture ratio. Under the conditions in Fig. 14, the capture ratio of $31.2 \pm 0.5\%$ was determined, which is

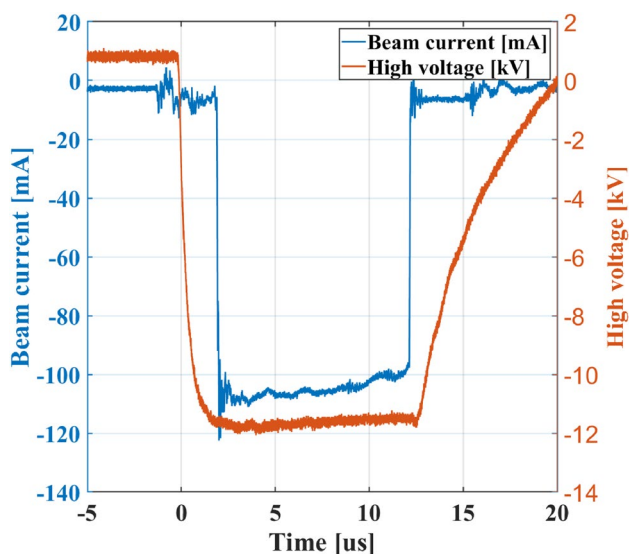


Fig. 14 (Color online) Signals of output beam current and high voltage applied on thermal DC gun

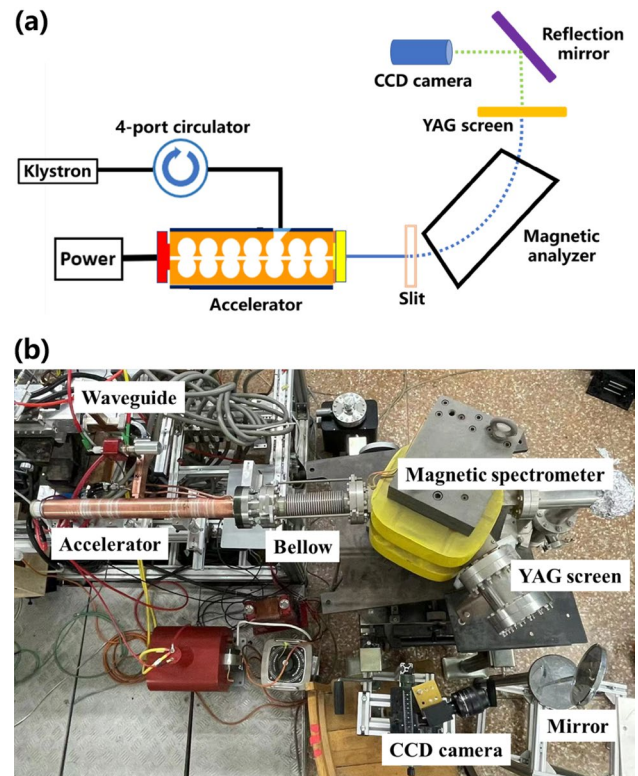


Fig. 15 (Color online) **a** Schematic of energy spread measurement experiment. **b** Image of energy spread measurement setup inside shielding room

just below the predicted value of 32% , possibly owing to processing and measurement errors.

A magnetic spectrometer was installed at the exit of the linear accelerator, as depicted in Fig. 15, to measure the beam energy spread. Further, to reduce the beam spot size and improve the energy resolution, a slit with the length of 38 mm and width of 0.2 mm was inserted at the entry of the magnetic spectrometer during the test. The size of the slit significantly affected the relative brightness of the screen, thereby affecting the energy resolution. With varying magnetic field, electrons with different kinetic energies exhibit unique drifting trajectories. The beam energy spread was evaluated based on the position and brightness of the YAG screen. The energy spectra of the output beams corresponding to different input powers are presented in Fig. 16. For the 2.4-MW input power, the kinetic energy of the output beam was 9.04 MeV , and the FWHM of the energy spectrum is approximately 3.5% .

A mirror was placed at the angle of 45° to the beamline, and the light was reflected from the YAG screen. A CCD camera with a focusing lens was used to capture images. The CCD camera has a resolution of approximately 50 m/px . The spot size of the output beam was estimated using an image on a YAG screen. The brightness distribution of the

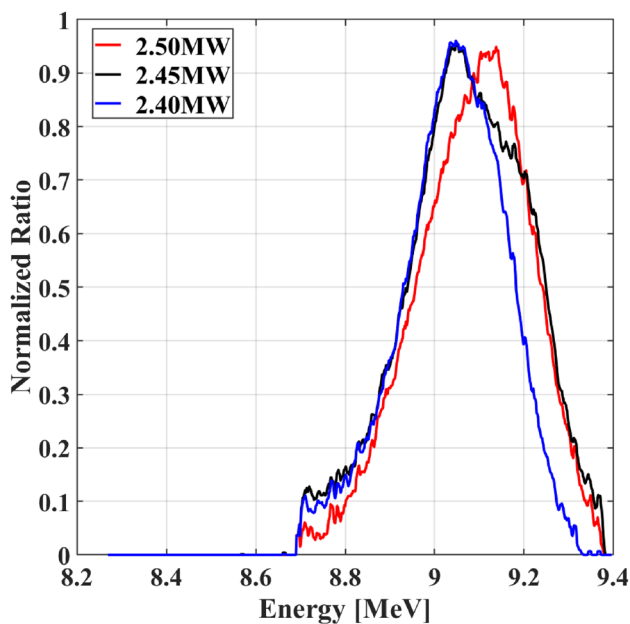


Fig. 16 (Color online) Energy spread measurement results with different input RF powers

images can be used to determine the RMS diameter of the beam because the brightness of the optical transition radiation is proportional to the number of incoming particles. For the input RF power of 2.4 MW and pulse beam current of 100 mA, the beam spot image was captured by the CCD camera, and the calculated RMS radius of the RMS beam spot was approximately 0.5 mm, as depicted in Fig. 17.

6 Conclusion

An X-band 9-MeV SW linear accelerator powered with a 2.4-MW klystron was developed at Tsinghua University. Its advantages include RF focusing without a solenoid, low-energy spread with a thermal DC gun, and no tuning pins.

SUPERFISH, CST, and ASTRA codes can be employed to facilitate redesign of the accelerator RF parameters, cavity geometry optimization, cavity chain RF simulation, and beam dynamics study. In addition, we conducted a low-power RF test after fabricating and tuning the copper disks. The results of the cold test and simulation are in good agreement.

A high-power RF experiment was further performed using an accelerator. During the high-power test, the output beam current, capture ratio, beam energy spectrum, and beam spot size were measured at the accelerator exit. With 2.4-MW input RF power, we obtained the pulse beam current of 100 mA and pulse width of approximately 9.8 μ s (under 0.1% duty factor). The output RMS spot radius was 0.5 mm and the output kinetic energy was 9.04 MeV, with

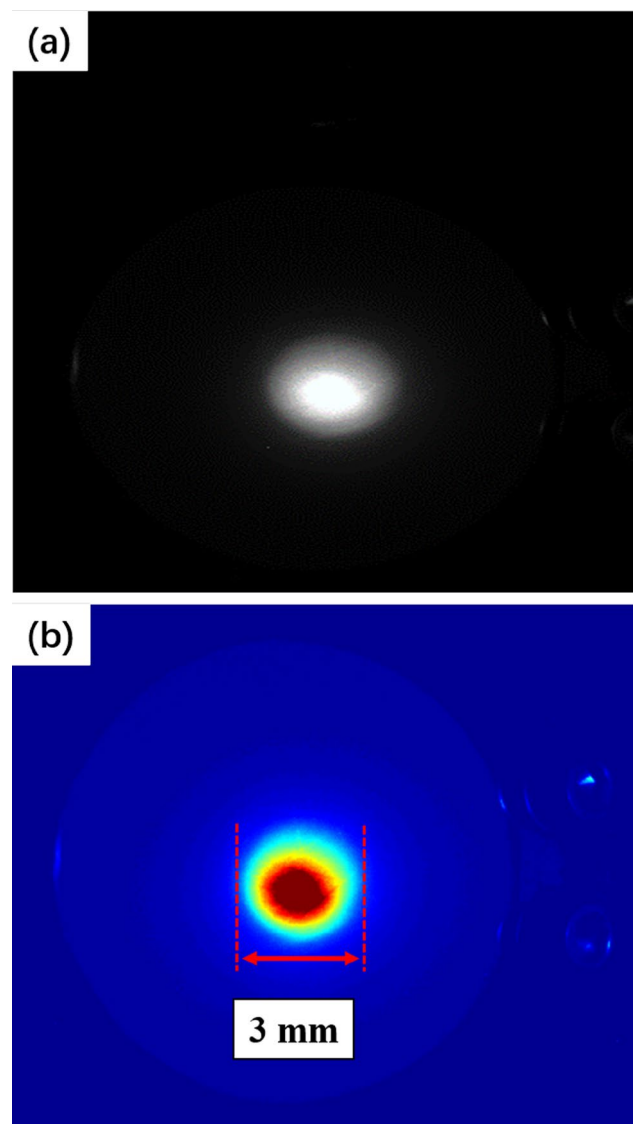


Fig. 17 (Color online) **a** Beam spot photo captured by CCD camera. **b** Brightness analysis result post-processing

the spectral FWHM of 3.5%. The results of the high-power RF experiment demonstrate the good performance of this accelerator. In the future, we will examine its performance with a high duty factor of 1. Further explorations will also be conducted regarding the proposed linear accelerator for higher-order modes.

Author contributions All authors contributed to the study conception and design. Material preparation, data collection, and analysis were performed by Jian Gao, Hao Zha, Jia-Ru Shi, Qiang Gao, Xian-Cai Lin, Fang-Jun Hu, Qing-Zhu Li, and Huai-Bi Chen. The first draft of the manuscript was written by Jian Gao, and all authors commented on the previous versions of the manuscript. All authors read and approved the final manuscript.

Data availability The data that support the findings of this study are openly available in Science Data Bank at <https://www.doi.org/10.>

57760/sciencedb.j00186.00117 and <https://cstr.cn/31253.11.sciencedb.j00186.00117>.

Declarations

Conflict of interest Jia-Ru Shi is an editorial board member for *Nuclear Science and Techniques* and was not involved in the editorial review, or the decision to publish this article. All authors declare that there are no competing interests.

References

1. C.X. Tang, Present status of the accelerator industry in Asia, in *Proceedings of the 1st International Particle Accelerator Conference, Kyoto, Japan*, 2010
2. E. Tanabe, A. Associates, Medical application of C-band accelerator technologies, in *Proceedings of the 19th International Linear Accelerator Conference, Chicago, USA*, 1998
3. C.X. Tang, H.B. Chen, Y. Liu et al., Low-energy linacs and their applications in Tsinghua university, in *Proceedings of the 23rd International Linear Accelerator Conference, Knoxville, USA*, 2006
4. Y. Kamino, S. Miura, M. Kokubo et al., Development of a new concept automatic frequency controller for an ultra-small C-band linear accelerator guide. *Med. Phys.* **34**, 1797 (2007). <https://doi.org/10.1118/1.2752581>
5. X.C. Lin, H. Zha, J.R. Shi et al., Fabrication, tuning, and high-gradient testing of an X-band traveling-wave accelerating structure for VIGAS. *Nucl. Sci. Tech.* **33**, 102 (2022). <https://doi.org/10.1007/s41365-022-01086-y>
6. J.H. Shao, H.B. Chen, Q.Z. Xing, Design of a C-band 6 MeV standing-wave linear accelerator structure, in *Proceedings of the 2nd International Particle Accelerator Conference, San Sebastian, Spain*, 2011
7. J.H. Shao, H. Zha, H.B. Chen, Fabrication and high power RF test of a C-band 6 MeV standing-wave linear accelerating structure, in *Proceedings of the 3rd International Particle Accelerator Conference, New Orleans, LA, USA*, 2012
8. J.H. Shao, H. Zha, H.B. Chen et al., High power test of a C-band 6 MeV standing-wave linear accelerator, in *Proceedings of the 4th International Particle Accelerator Conference, Shanghai, China*, 2013
9. J.H. Shao, Y.C. Du, H. Zha et al., Development of a C-band 6 MeV standing-wave linear accelerator. *Phys. Rev. Accel. Beams.* **16**, 090102 (2013). <https://doi.org/10.1103/PhysRevSTAB.16.090102>
10. C.M. Ma, S.B. Jiang, Monte Carlo modelling of electron beams from medical accelerators. *Phys. Med. Biol.* **44**, 157 (1999). <https://doi.org/10.1088/0031-9155/44/12/201>
11. <https://www.cst.com>
12. <https://www.desy.de/~mpyflo/>
13. J. Shi, Studies of RF deflecting/crab cavities for beam manipulation and diagnostics. Dissertation, Tsinghua University, Beijing, 2009 (in Chinese)
14. T.P. Wangler, *RF linear accelerators* (Wiley, Hoboken, 2008)
15. X.C. Lin, H. Zha, J.R. Shi et al., Development of a 7-cell S-band standing-wave RF-deflecting cavity for Tsinghua Thomson scattering X-ray source. *Nucl. Sci. Tech.* **32**, 36 (2021). <https://doi.org/10.1007/s41365-021-00871-5>
16. X.C. Lin, H. Zha, J.R. Shi et al., Design, fabrication, and testing of low-group-velocity S-band traveling-wave accelerating structure. *Nucl. Sci. Tech.* **33**, 147 (2022). <https://doi.org/10.1007/s41365-022-01124-9>
17. J. Shi, A. Grudiev, A. Olyunin et al. Tuning of CLIC accelerating structure prototypes at CERN, in *Proceedings of the 28th International Linear Accelerator Conference, Tsukuba, Japan*, (2010)
18. J. Shi, A. Grudiev, W. Wuensch, Tuning of X-band traveling-wave accelerating structures. *Nucl. Instrum. Meth. A.* **704**, 14 (2013). <https://doi.org/10.1016/j.nima.2012.11.182>
19. M.M. Peng, J.R. Shi, H. Zha et al., Development and high-gradient test of a two-half accelerator structure. *Nucl. Sci. Tech.* **32**, 60 (2021). <https://doi.org/10.1007/s41365-021-00895-x>
20. V. Dolgashev, Study of basic breakdown phenomena in high gradient vacuum structures. in *Proceedings of Linear Accelerator Conference, LINAC2010, Tsukuba, Japan*, 2010
21. V. Dolgashev, S. Tantawi, Y. Higashi et al., Geometric dependence of radio-frequency breakdown in normal conducting accelerating structures. *Appl. Phys. Lett.* **97**, 171501 (2010). <https://doi.org/10.1063/1.3505339>
22. A. Grudiev, W. Wuensch, S. Calatroni, New local field quantity describing the high gradient limit of accelerating structures. *Phys. Rev. Spec. Top-Ac.* **12**, 102001 (2009). <https://doi.org/10.1103/PhysRevSTAB.12.102001>
23. A. Degiovanni, W. Wuensch, G.N. Jorge, Comparison of the conditioning of high gradient accelerating structures. *Phys. Rev. Accel. Beams.* **19**, 032001 (2016). <https://doi.org/10.1103/PhysRevAccelBeams.19.032001>

Springer Nature or its licensor (e.g. a society or other partner) holds exclusive rights to this article under a publishing agreement with the author(s) or other rightsholder(s); author self-archiving of the accepted manuscript version of this article is solely governed by the terms of such publishing agreement and applicable law.